Supplementary Information file: Role of microstructure in the lattice thermal conductivity and thermoelectric performance of $Cu_{2+y}Zn_{1-y}SnS_xSe_{4-x}$ alloys

Marcelo Augusto Malagutti[a], Eleonora Isotta[a]*, Himanshu Nautiyal[b], Umberto Anselmi-Tamburini[c], Andrea Chiappini[d], Sebastian Bette[e], Robert Dinnebier[e], Narges Ataollahi[a], Paolo Scardi[a]*

[a]*Department of Civil, Environmental and Mechanical Engineering, University of Trento, Via Mesiano 77, 38123, Trento, Italy*

[b]*Department of Physics, School of Physical and Biological Sciences, Manipal University Jaipur, Jaipur 303007, Rajasthan, India*

[c]*Department of Chemistry, University of Pavia, Pavia, Italy*

[d]*Institute of Photonics and Nanotechnologies (IFN-CNR) CSMFO Laboratory and Fondazione Bruno Kessler (FBK) Photonics Unit, Via Alla Cascata 56/C, 39123 Trento, Italy*

[e]*Max Planck Institute for Solid State Research, Heisenbergstrasse 1, 170569, Stuttgart, Germany*

Corresponding authors: eleonora.isotta@gmail.com, paolo.scardi@unitn.it

Supplementary Note 1: Rietveld Analysis

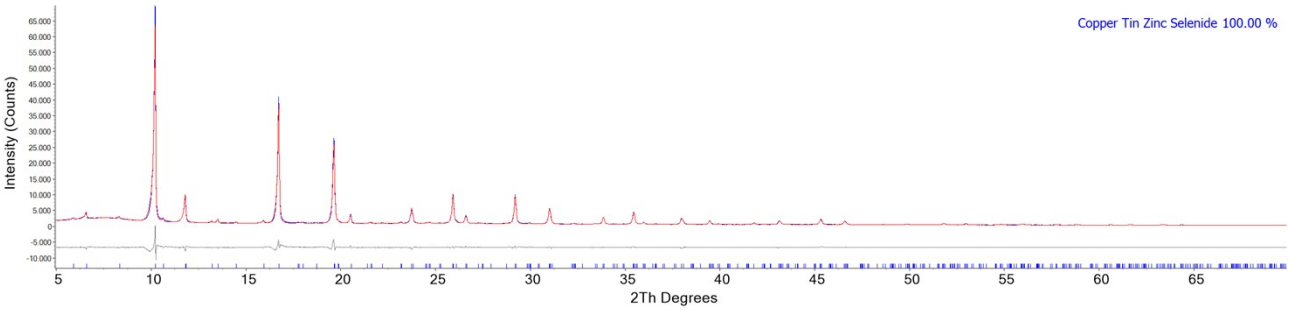

Figure S 1. Rietveld Analysis of the Cold-Pressed $Cu_{2.125}Zn_{0.875}SnS_4$. Blue line corresponds to experimental data obtained from AgKα radiation, red line represents the profile modelling, and gray the residuals. The blue markers correspond to the crystallographic Miller indices.

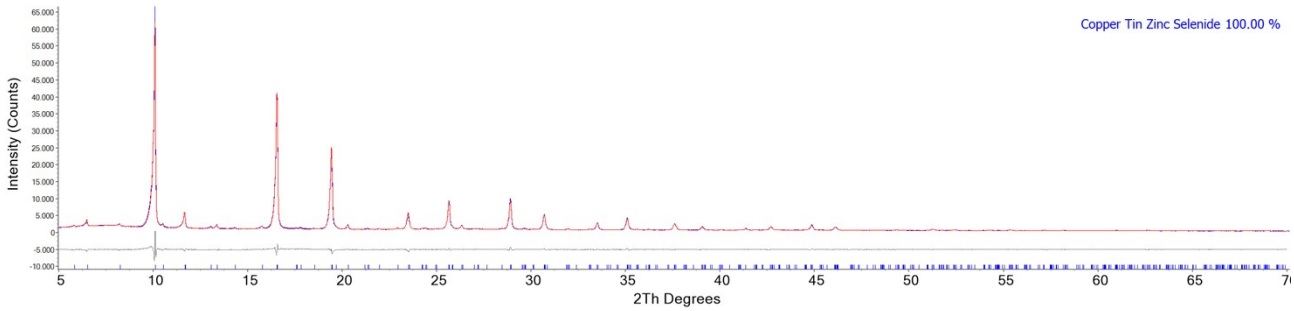

Figure S 2. Rietveld Analysis of the Cold-Pressed $Cu_{2.125}Zn_{0.875}SnS_3Se_1$. Blue line corresponds to experimental data obtained from AgKα radiation, red line represents the profile modelling, and gray the residuals. The blue markers correspond to the crystallographic Miller indices.

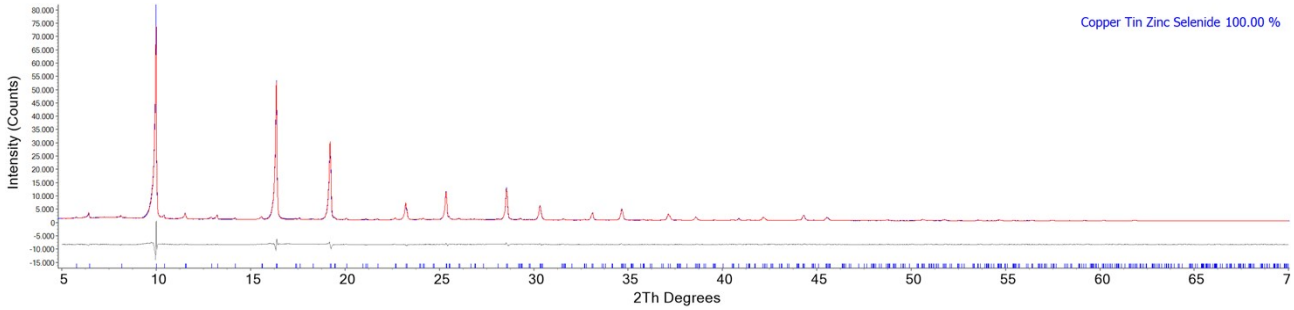

Figure S 3. Rietveld Analysis of the Cold-Pressed $Cu_{2.125}Zn_{0.875}SnS_2Se_2$. Blue line corresponds to experimental data obtained from AgKα radiation, red line represents the profile modelling, and gray the residuals. The blue markers correspond to the crystallographic Miller indices.

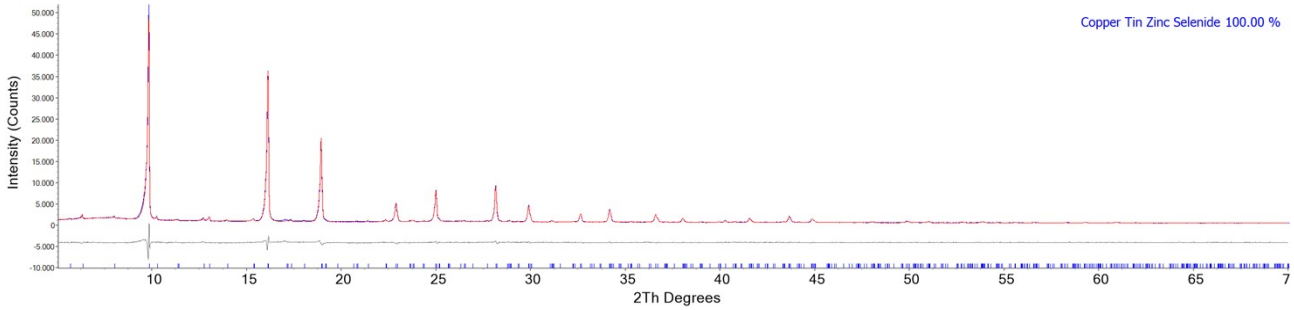

Figure S 4. Rietveld Analysis of the Cold-Pressed $Cu_{2.125}Zn_{0.875}SnS_1Se_3$. Blue line corresponds to experimental data obtained from AgKα radiation, red line represents the profile modelling, and gray the residuals. The blue markers correspond to the crystallographic Miller indices.

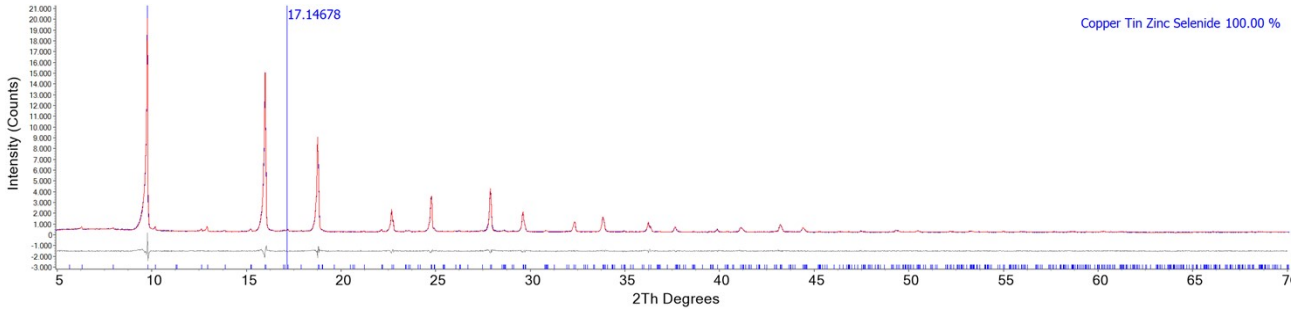

Figure S 5. Rietveld Analysis of the Cold-Pressed $Cu_{2.125}Zn_{0.875}SnSe_4$. Blue line corresponds to experimental data obtained from AgKα radiation, red line represents the profile modelling, and gray the residuals. The blue markers correspond to the crystallographic Miller indices.

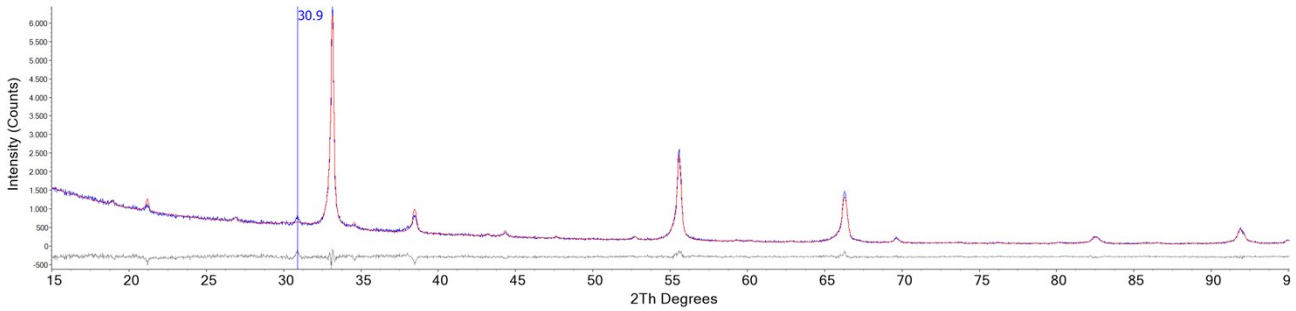

Figure S 6. Rietveld Analysis of the SPS $Cu_{2.125}Zn_{0.875}SnS_4$. Blue line corresponds to experimental data obtained from AgKα radiation, red line represents the profile modelling, and gray the residuals. The vertical line corresponds to C electrode employed for the SPS contact.

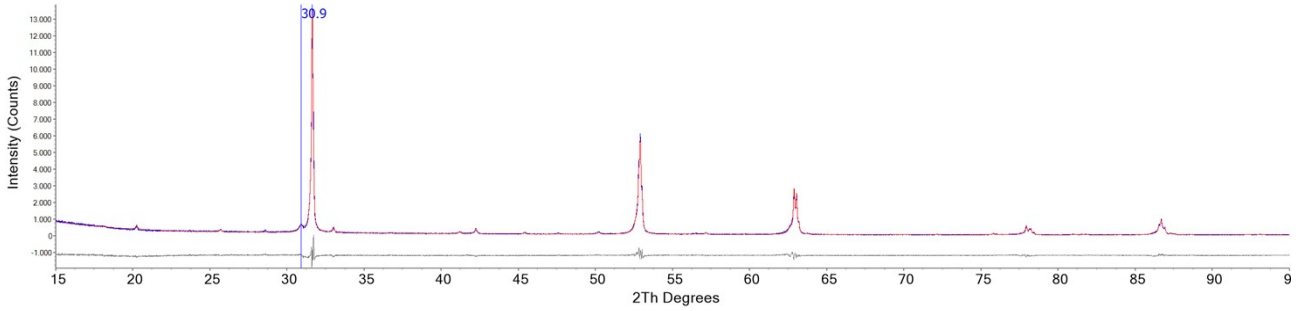

Figure S 7. Rietveld Analysis of the SPS $Cu_{2.125}Zn_{0.875}SnSe_4$. Blue line corresponds to experimental data obtained from AgKα radiation, red line represents the profile modelling, and gray the residuals. The vertical line corresponds to C electrode employed for the SPS contact.

Supplementary Note 2: Raman analysis of the cold-pressed samples

The Cu_{Zn} substitutions can be better observed via Raman analysis that are given in Figure S 8. For CZTSe, the increase on this type of substitution leads to the increase in the peak around 190 cm^{-1} [1]. In addition, the deviation from stoichiometry shifts the main 194 cm^{-1} to higher values, in this case 197 cm^{-1}, due to the excess of Cu [2] (vide Figure S 8(a)). For CZTS, the main A modes are identifyed at 337 cm^{-1} and 287 cm^{-1} [3] as shown in Figure S 8(b). The other peaks are indexed as longitudinal optical modes (LO) of the polar B and E components [4]. In addition, the increased anion disorder for $x = 1, 2, 3$ broadens the Raman peaks as showcased in Figure S 8(c). Extracting the Vegard relations for the Se and S bonds from the Raman spectra, the relation are shown in Figure S 8. In this case, the point of x = 3 was not used since it deviates from the correct stoichiometry (vide EDX results in Table S 1). A similar relation is found compared to the literature for the Se bonds, but significantly deviate for the S bonds (see Figure S 8(d)) [3]. The deviation from linearity is also observed in recent reports and was credited to small fluctuation of the stoichiometry in this proportion region.

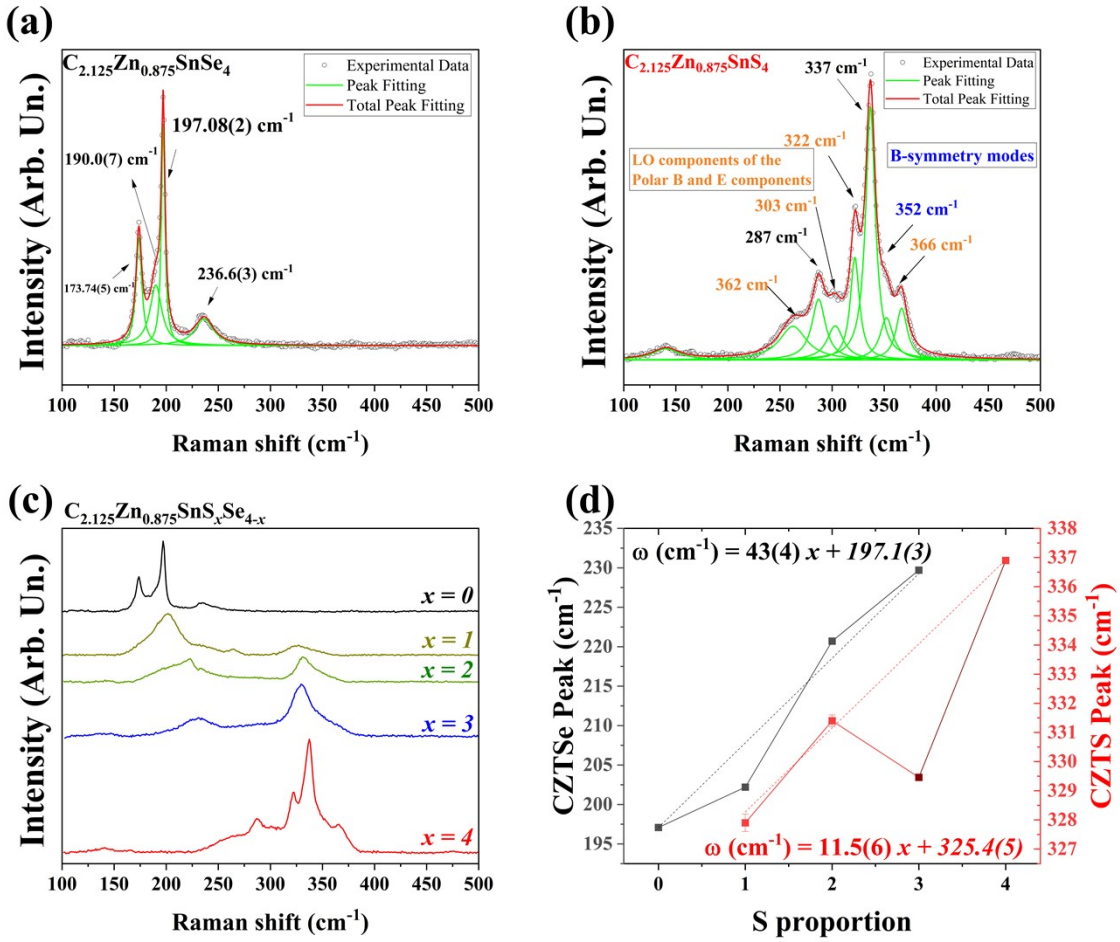

Figure S 8. Raman spectra of the (a) $Cu_{2.125}Zn_{0.875}SnSe_4$ and (b) $Cu_{2.125}Zn_{0.875}SnS_4$ samples fabricated by cold-pressing and sintered at 883 K. Dots represent the experimental data, green line the Raman peaks, and the red line the summed contribution of each peak. (c) Raman spectra of the entire $Cu_{2.125}Zn_{0.875}SnS_xSe_{4-x}$ series. (d) Vegard relations for the Se (black) and S (red) -cation bonds.

Supplementary Note 3: mode Gruneisen parameter

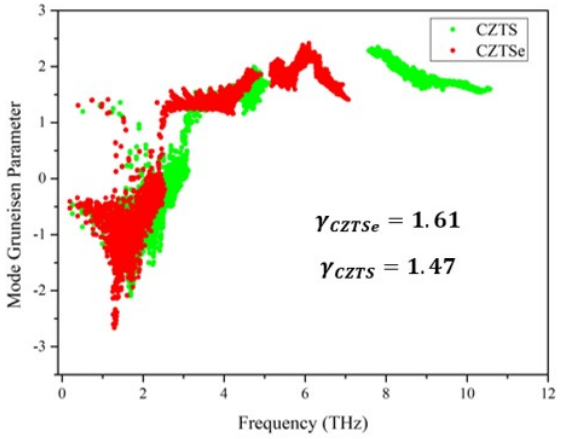

Figure S 9. Gruneisen parameter vs frequency plots for CZTS and CZTSe obtained via DFPT.

Supplementary Note 4: Electron microscopy analysis

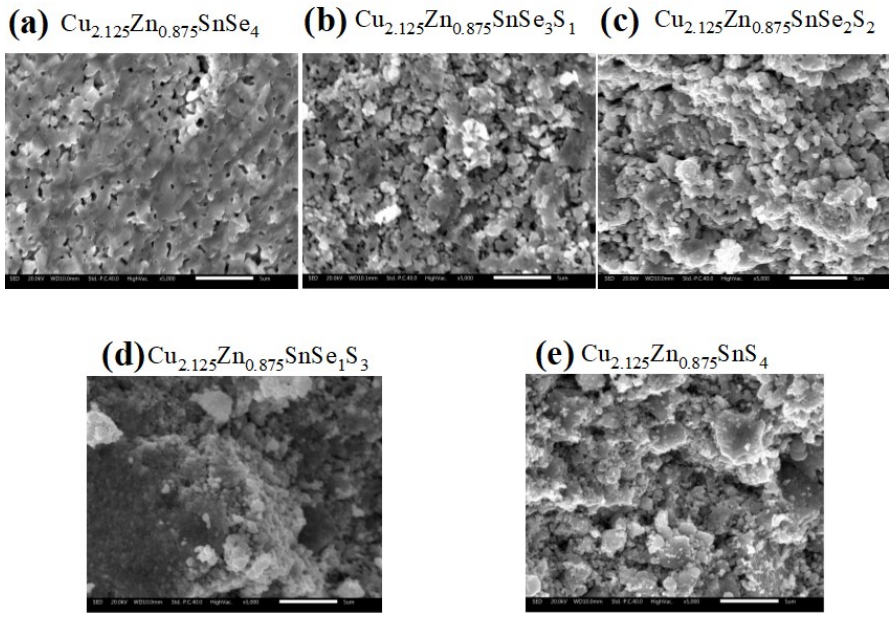

Figure S 10. SEM analysis for the cold -pressed samples.

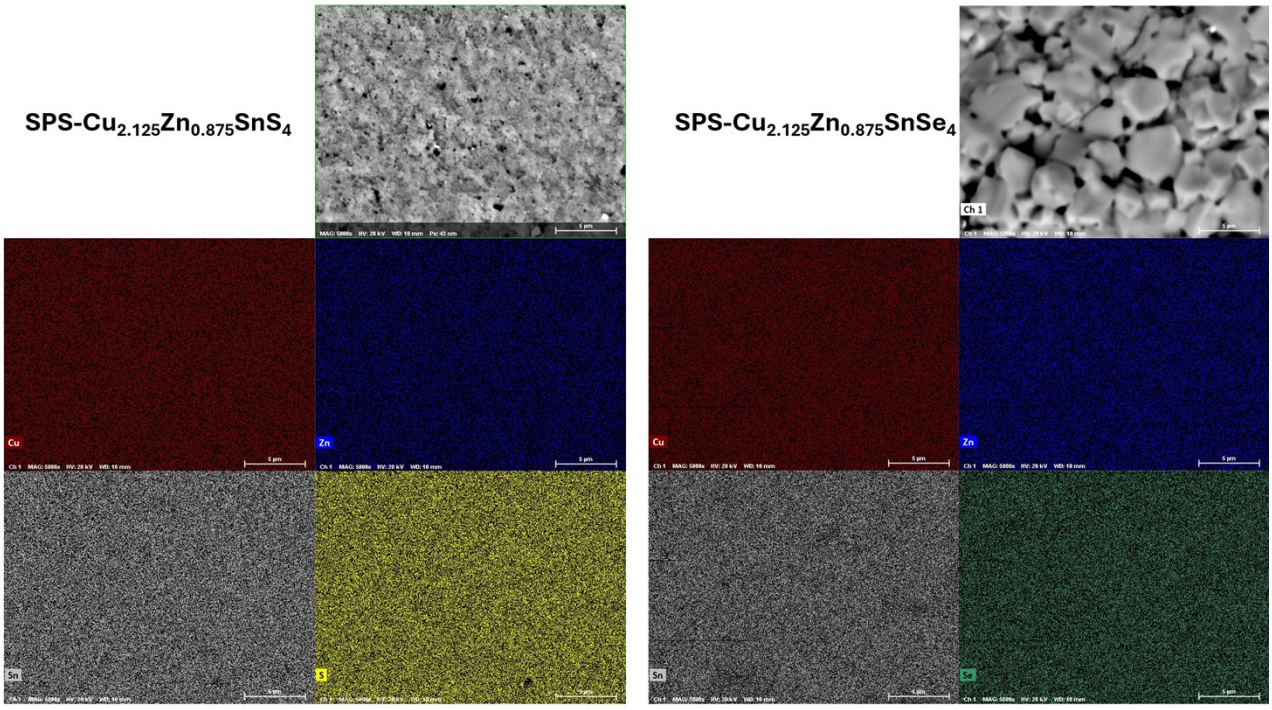

Figure S 11. SEM and chemical maps for the SPS CZTSSe samples.

Table S 1. EDS analysis of the $Cu_{2.125}Zn_{0.875}SnS_xSe_{4-x}$ fold cold pressed and SPS samples. The ideal proportion of Cu/Zn = 2.43. Measurement performed at the centre of the cross-section of the cold-pressed disk. Φ corresponds to the pore fraction.

x	Φ	Cu %	Zn %	Sn %	S %	Se %	Cu/Zn	S/(S+Se)	Anion/Cation Ratio
					Cold pressed samples				
0	22%	26.9(6)	10.6(3)	12.6(6)	-	50(1)	2.5	0	0.9979
1	22%	26.9(6)	11.0(3)	12.8(6)	12.1(2)	37(1)	2.44	0.25	0.9708
2	16%	26.6(7)	11.4(3)	13.1(7)	25.9(5)	23.0(8)	2.33	0.53	0.9615
3	35%	29.9(8)	10.0(3)	11.5(7)	38.9(8)	9.6(4)	2.99	0.8	0.9433
4	32%	28.6(10)	13.0(5)	13.0(9)	45(1)	-	2.2	1	0.8333
					SPS samples				
0	3%	26.9(6)	11.0(3)	11.7(6)	-	50.5(1)	2.45	0	1.02
4	9%	26.7(10)	10.8(3)	12.0(9)	50.4(1)	-	2.46	1	1.02

Supplementary Note 5: microstrain analysis

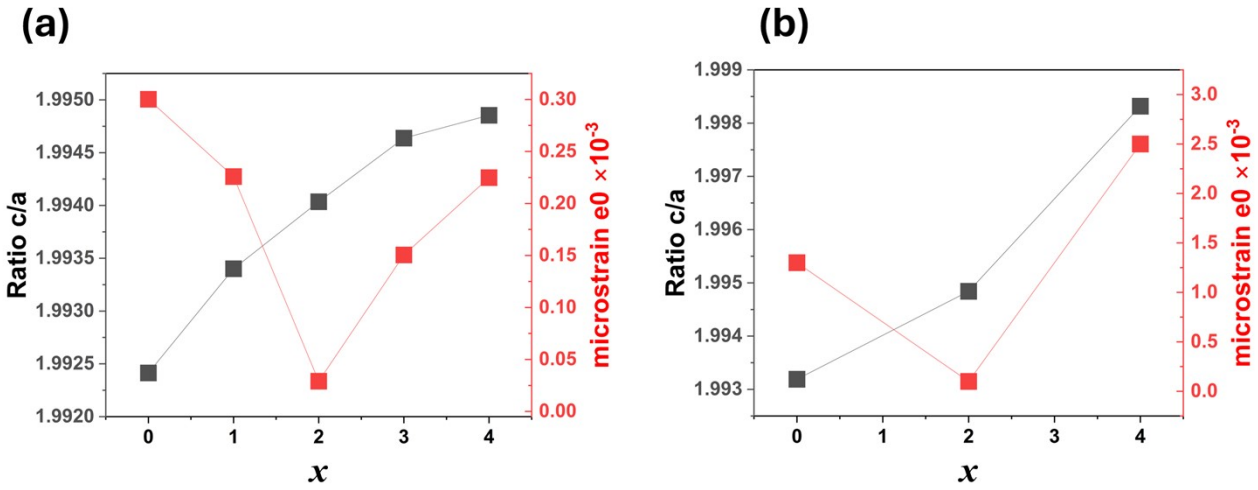

Figure S 12. Ratio of the lattice parameters c/a and microstrain for (a) cold-pressed and (b) SPS samples.

Supplementary Note 6: crystallite and grain size analysis

The crystallite size distribution is modelled via whole powder pattern approach (WPPM) using the macros available for the TOPAS software [5–7]. It utilizes a log-normal distribution of spheres, where the log-normal mean and standard deviation are refined. For details follow details here: https://topas.webspace.durham.ac.uk/tutorial-wppm/.

The average grain size was estimated from SEM micrographs using the line intercept method. A set of straight test lines was superimposed on each calibrated micrograph in multiple orientations to minimize directional bias. For each line, the number of intersections with grain boundaries was counted, and the true line length was measured. The mean lineal interception length was calculated as the ratio between the total test line length and the number of grain-boundary interceptions, providing an estimate of the average grain size along that direction. The values obtained from several lines were averaged to determine the mean grain size and corresponding standard deviation. The ASTM-equivalent grain diameter was then calculated from the mean intercept length to allow comparison between samples. This stereological approach provides a statistically representative estimate of grain size, particularly suitable for irregular and porous microstructures. Values and representation is given in Figure S 13.

Size estimation via SEM

Line intercept method

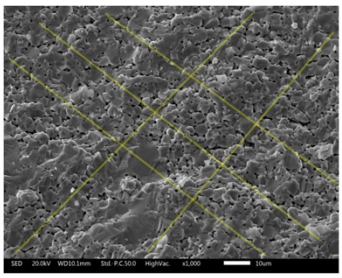

SPS

S4_X_SED_2_0005.Tif

Line	Length (nm)	Number of Intercepts	Grain Size (nm)
1	6215.215	23	270.2267391
2	5410.615	20	270.53075
3	4194.833	19	220.7806842
4	15211.15	48	316.8989583
5	14223.987	44	323.2724318
6	10596.496	37	286.3917838
Average			281.3502245
Standard Deviation			37.2989636
ASTM average grain diameter			438.9063503
ASTM std. grain diameter			58.18638322

Se4_X_SED_2_0001.Tif

Line	Length (nm)	Number of Intercepts	Grain Size (nm)
1	147473.667	38	3880.885974
2	147194.268	48	3066.54725
3	110346.84	39	2829.406154
4	109018.576	35	3114.816457
5	68342.319	26	2628.550731
Average			3104.041313
Standard Deviation			476.0581109
ASTM average grain diameter			4842.304448
ASTM std. grain diameter			742.650653

Cold-Pressed

Cu2p125Zn0p875SnS4_X_SED_2_0001

Line	Length (nm)	Number of Intercepts	Grain Size (nm)
1	10810.927	27	400.4047037
2	9801.165	28	350.0416071
3	16699.745	29	575.8532759
4	9732.963	31	313.9665484
5	28348.23	63	449.9719048
6	10935.055	20	546.75275
Average			439.498465
Standard Deviation			105.3517183
ASTM average grain diameter			685.6176054
ASTM std. grain diameter			164.3486805

Cu2p125Zn0p875SnSe4_X_SED_2_0001.Tif

Line	Length (nm)	Number of Intercepts	Grain Size (nm)
1	29449.844	42	701.1867619
2	27482.744	29	947.6808276
3	24462.494	27	906.0182963
4	18367.036	18	1020.390889
5	14934.122	13	1148.778615
Average			944.811078
Standard Deviation			164.454391
ASTM average grain diameter			1473.905282
ASTM std. grain diameter			256.54885

Figure S 13. Results obtained with the line intercept method for the SPS and cold-pressed samples.

Supplementary Note 7: Performance of tetragonal phases

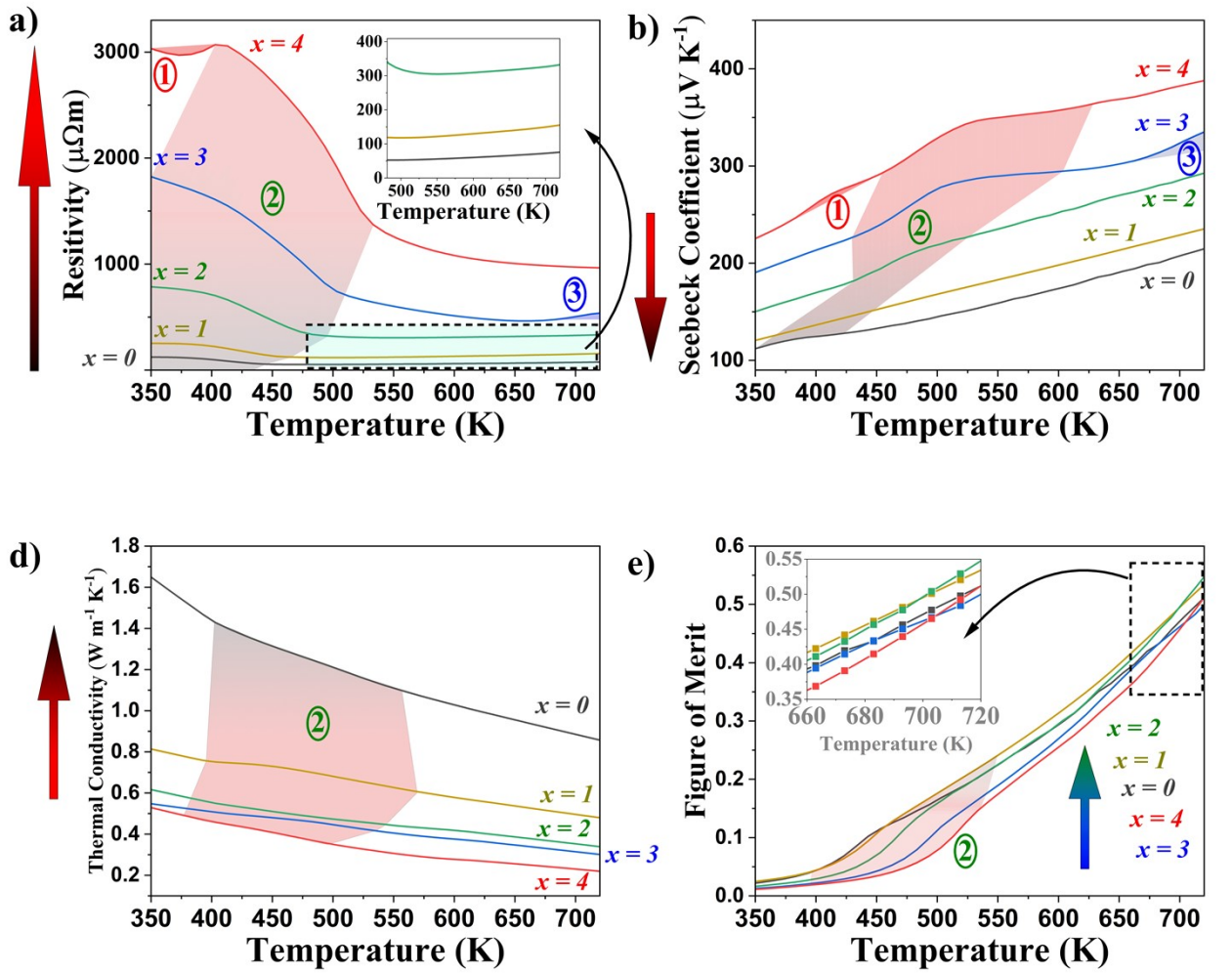

Figure S 14. (a) Resisitivity, (b) Seebeck coefficient, (c) thermal conductivity, and (d) Figure of merit for the $Cu_{2.125}Zn_{0.875}SnS_xSe_{4-x}$ series.

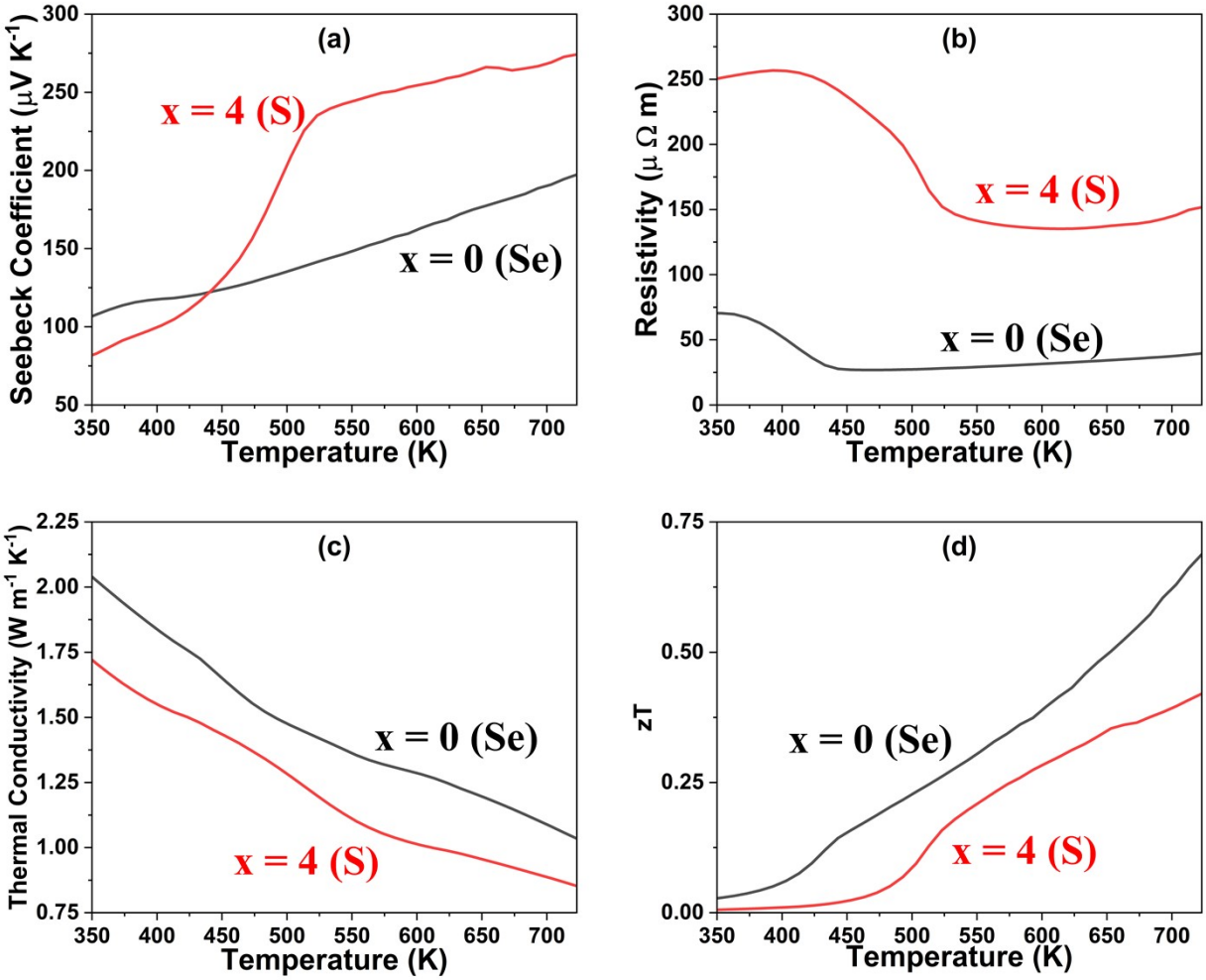

Figure S 15. (a) Resisitivity, (b) Seebeck, (c) thermal conductivity, and (d) Figure of merit for the $Cu_{2.125}Zn_{0.875}SnS_xSe_{4-x}$ series.

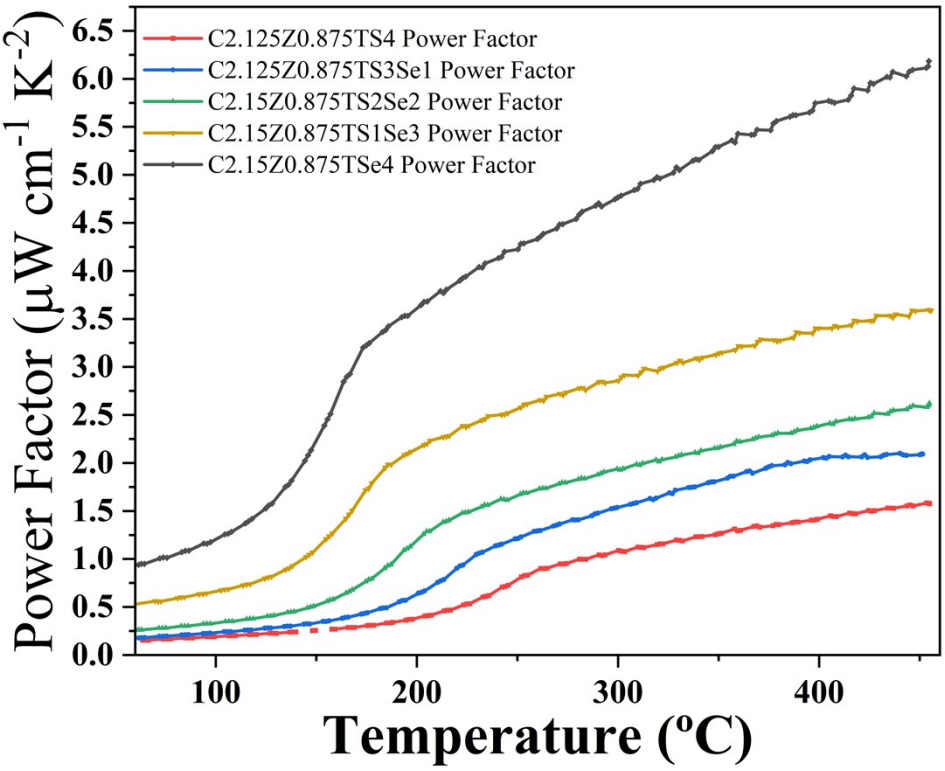

Figure S 16. Power factor obtained for the cold pressed samples.

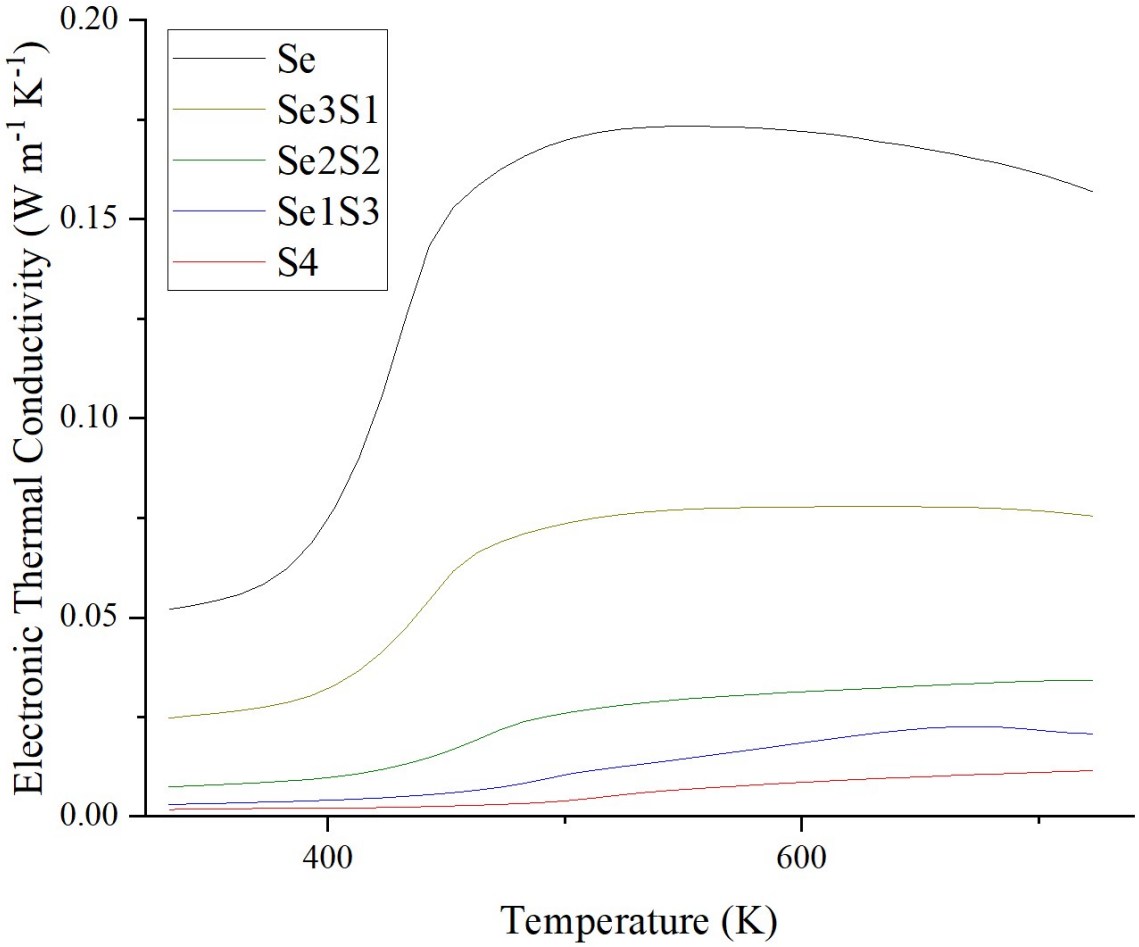

Figure S 17. Electronic thermal conductivity for the cold-pressed samples.

Supplementary Note 8: DFT analysis

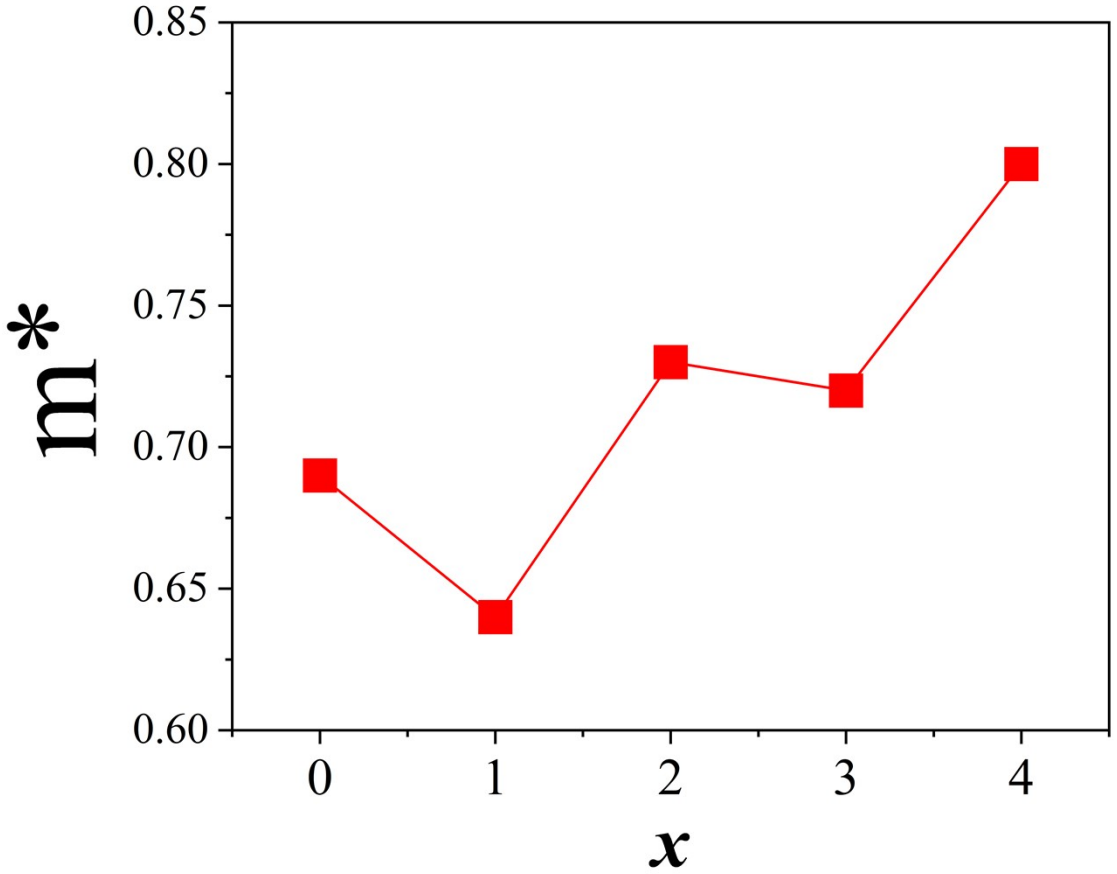

Figure S 18. DFT density of states effective mass.

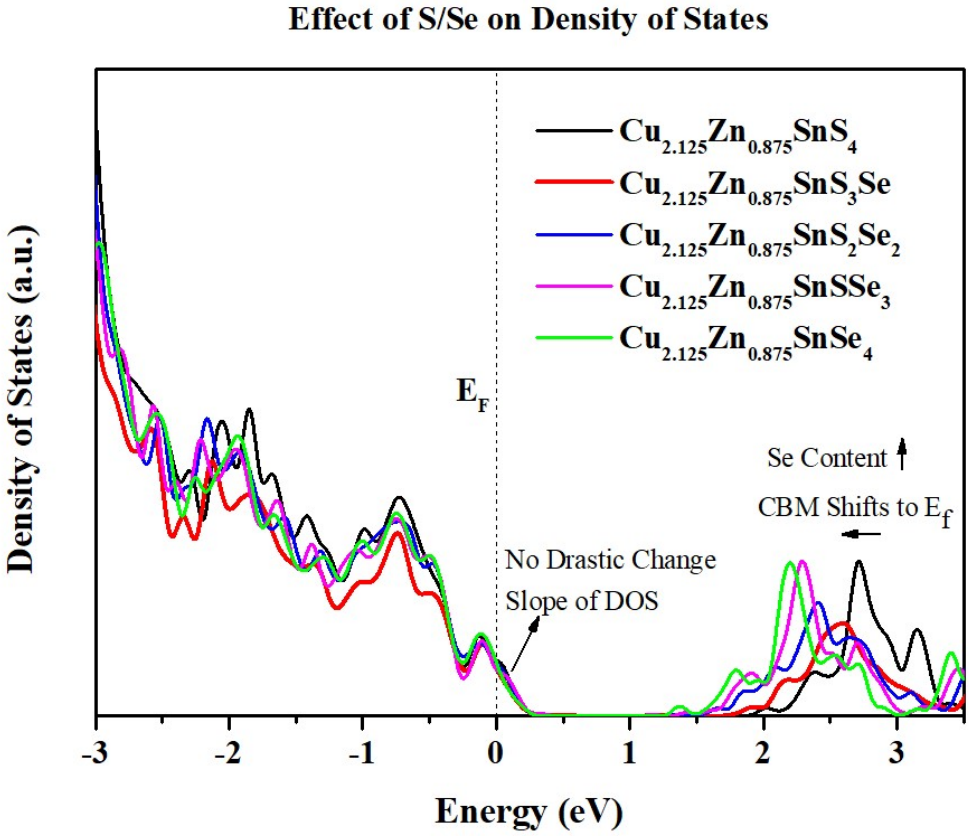

Figure S 19. DFT density of states.

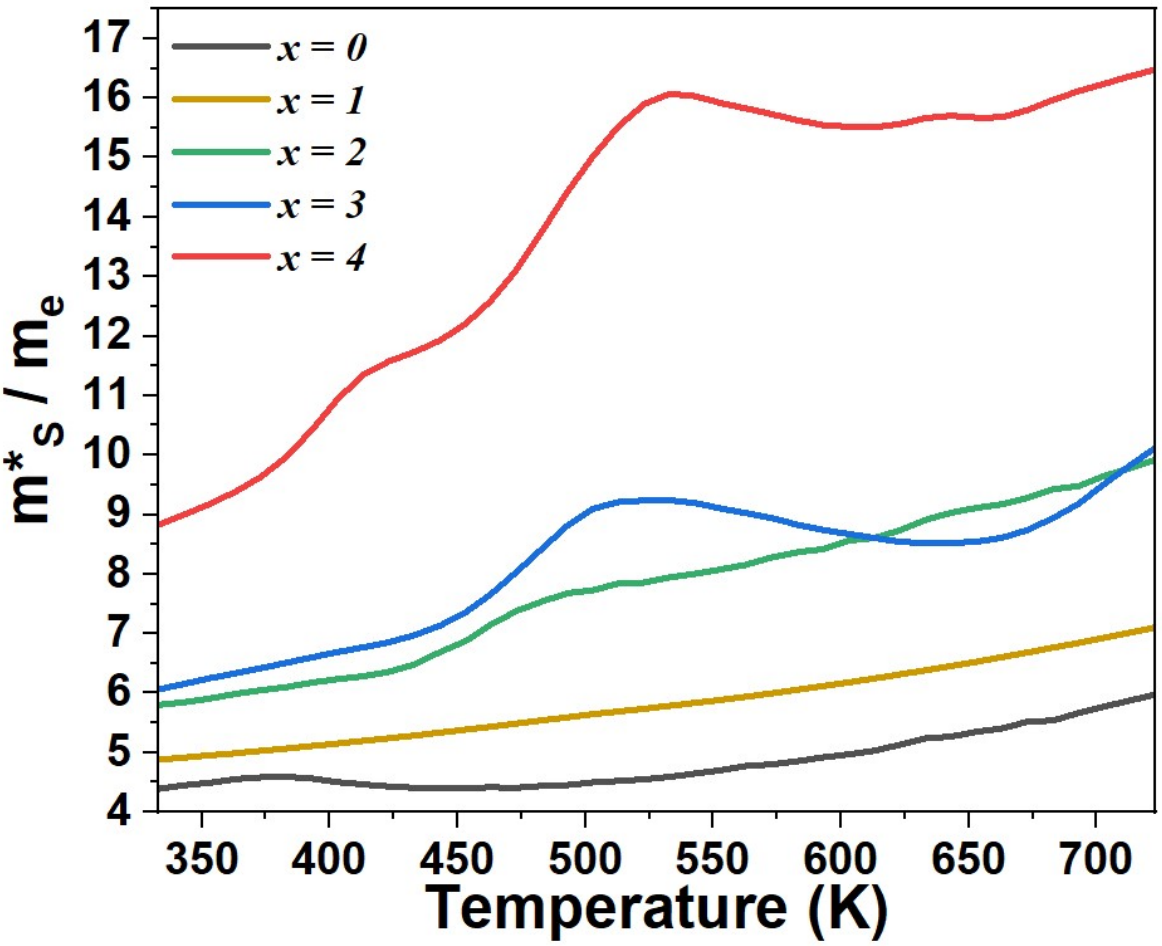

Figure S 20. Seebeck effective mass of the charge carriers.

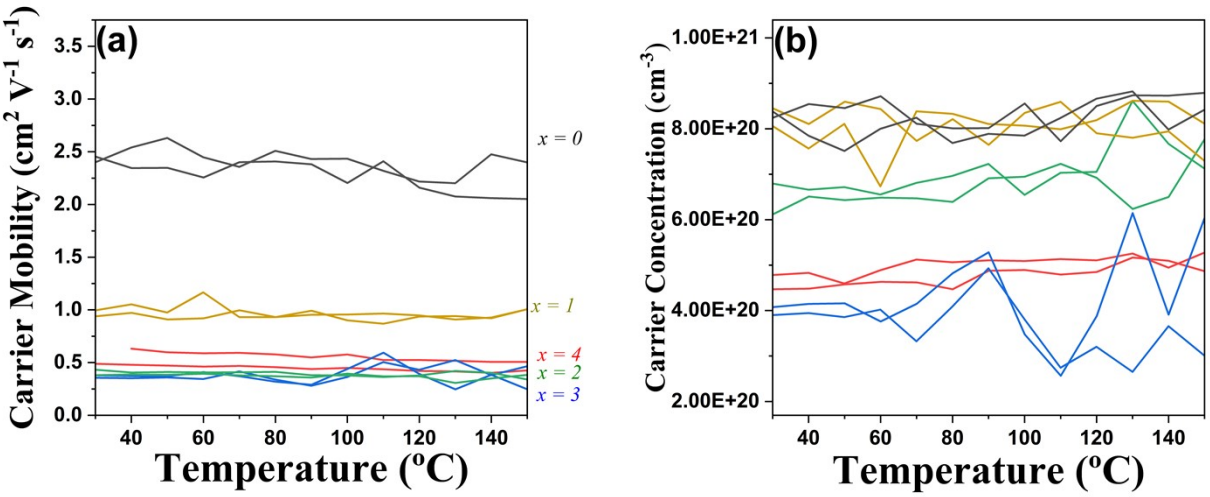

Figure S 21. Hall effect measurements of (a) carrier mobility and (b) carrier concentration for the cold-pressed samples.

Supplementary Note 9: Debye-Callaway model

Debye Callaway equations rule including all the possible scattering mechanisms [1–3] in the form:

$$\kappa_l = \frac{1}{3}\int_0^{\omega_{max}} C_s(\omega) v_g(\omega)^2 \tau(\omega) d\omega$$

Where the maximum phonon frequency is given by

$$\omega_{max} = \left(\frac{6\pi^2}{V}\right)^{1/3} v_{sound}$$

Being V the volume of the unit cell, and v_{sound} the average speed of sound between longitudinal and transverse modes. Here the phonon group speed is approximated as the speed of sound, i.e., $v_g(\omega) = v_{sound}$. At high temperatures, the spectral heat capacity ($C_s(\omega)$) can be approximated as: $C_s(\omega) = \frac{3k_B\omega^2}{2\pi^2 v_{sound}^3}$

k_B is the Boltzmann constant. The phonon relaxation time is modelled by a combination of Umklapp (τ_U), grain-boundary (τ_{GB}), and point defects (τ_{PD}) in the form

$$\tau^{-1} = \sum_i \tau_i^{-1}$$

Umklapp scattering models the phonon scattering by the following frequency dependency:

$$\tau_U(\omega) = \frac{(6\pi^2)^{1/3}}{2} \frac{\bar{M} v_{sound}^3}{k_B V^{1/3} \gamma^2 \omega^2 T}$$

Where $\bar{M}$ is the average atomic mass and γ the Gruneisen parameter. Grain-boundary scattering is governed by the following relaxation time: $\tau_{GB} = \frac{d}{v_{sound}}$

Where d is the SEM or XRD particle/domain size.

Point defects are modelled with both mass (m_i) and atomic radius (r_i) fluctuations residing on site with average mass and radius $\bar{m}$ and $\bar{r}$, respectively:

$$\tau_{PD} = \frac{V\omega^4}{4\pi v_{sound}^3}\left[\sum_i f_i\left(1-\frac{m_i}{\bar{m}}\right)^2 + \sum_i f_i\left(1-\frac{r_i}{\bar{r}}\right)^2\right]$$

The fluctuation is modelled by the occupancy fraction f_i. For vacancies, the mass of the point defects is null and we decided to omit the strain contribution

To understand the temperature dependency for the materials, we model the matrix thermal conductivity (κ_{matrix}) for the SPS samples. Since they contain no vacancies defects, only Umklapp and grain-boundary effects are modelled. The results are shown in Figure S 22. To fit well the data, the κ_l was multiplied by a constant value

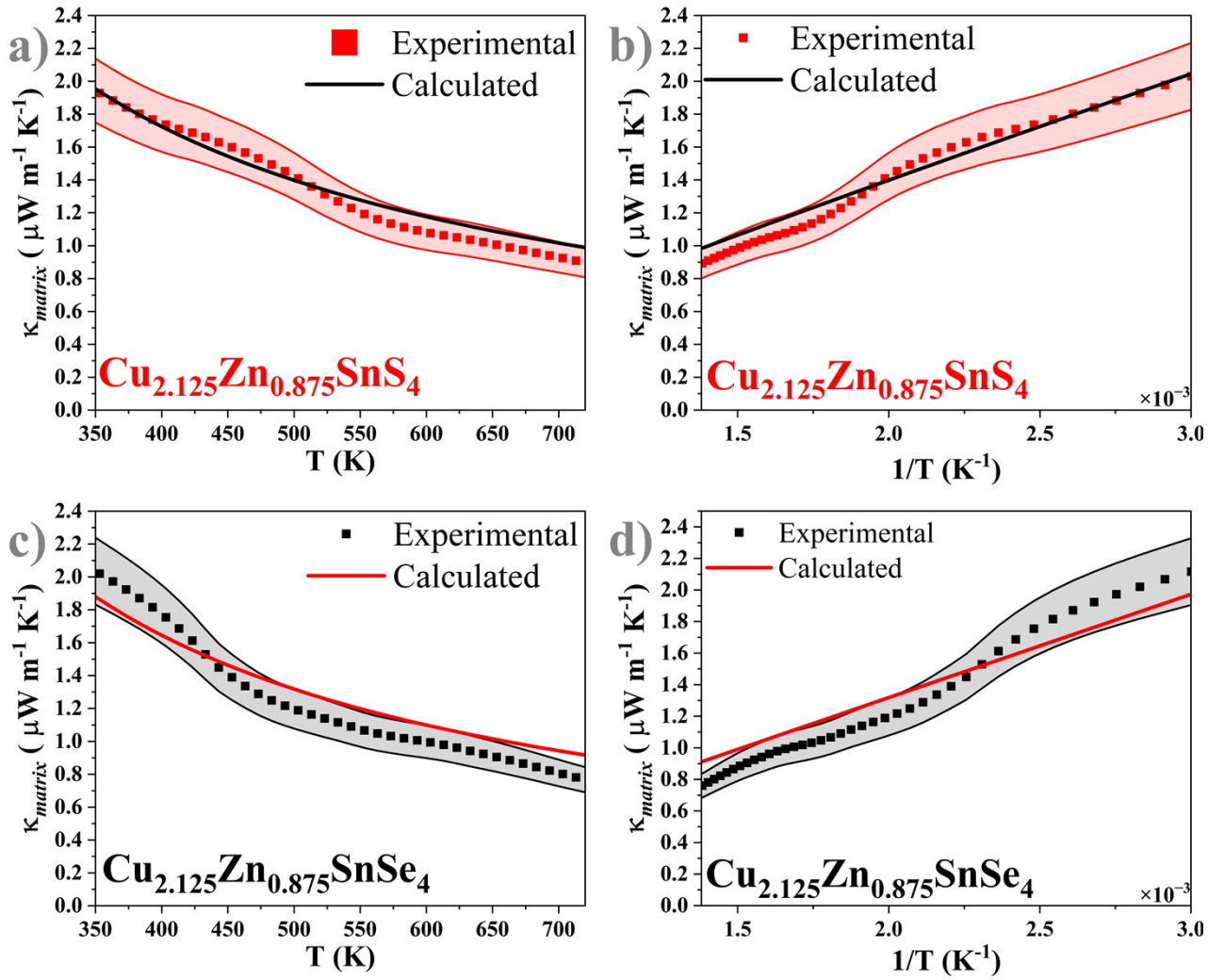

Figure S 22. Fitting of the lattice thermal conductivity using the Debye–Callaway model, considering grain-boundary and Umklapp scattering contributions to the relaxation times. Panels (a) and (b) show the fitting results for $Cu_{2.125}Zn_{0.875}SnS_4$ plotted as a function of temperature (T) and its inverse (T^{-1}), respectively. Panels (c) and (d) present the corresponding plots for $Cu_{2.125}Zn_{0.875}SnSe_4$. Error bars were estimated at 10% and define the contour curves surrounding the experimental data (symbols). The model predictions are shown as solid lines.

References

[1] Y.A. Romaniuk, I.S. Babichuk, V. V. Korotyeyev, V.O. Yukhymchuk, V.M. Dzhagan, S. V. Virko, M.O. Semenenko, M.O. Stetsenko, A. Tiutiunnyk, L.M. Pérez, D. Laroze, Sci. Rep. 15 (2025) 1–17.

[2] M. Dimitrievska, A. Fairbrother, E. Saucedo, A. Pérez-Rodríguez, V. Izquierdo-Roca, Appl. Phys. Lett. 106 (2015).

[3] T.D.C. Hobson, O.S. Hutter, N. Fleck, L.M. Daniels, J.D. Major, T.M. Ng, K. Durose, Cryst. Growth Des. 20 (2020) 2164–2173.

[4] M. Guc, S. Levcenko, V. Izquierdo-Roca, X. Fontané, E. Arushanov, A. Pérez-Rodríguez, J. Appl. Phys. 114 (2013).

[5] P. Scardi, C.L. Azanza Ricardo, C. Perez-Demydenko, A.A. Coelho, J. Appl. Crystallogr. 51 (2018) 1752–1765.

[6] P. Scardi, M. Leoni, Acta Crystallogr. Sect. A Found. Crystallogr. 58 (2002) 190–200.

[7] P. Scardi, M. D'Incau, M.A. Malagutti, M.W. Terban, B. Hinrichsen, A.N. Fitch, J. Appl. Crystallogr. 58 (2025) 1764–1777.